

# Pentagon, Hexagon, or Bridge? Identifying the Location of a Single Vanadium Cation on Buckminsterfullerene Surface

Jianzhi Xu, Joost M. Bakker, Olga V. Lushchikova, Peter Lievens, Ewald Janssens,\* and Gao-Lei Hou\*



Cite This: *J. Am. Chem. Soc.* 2023, 145, 22243–22251



Read Online

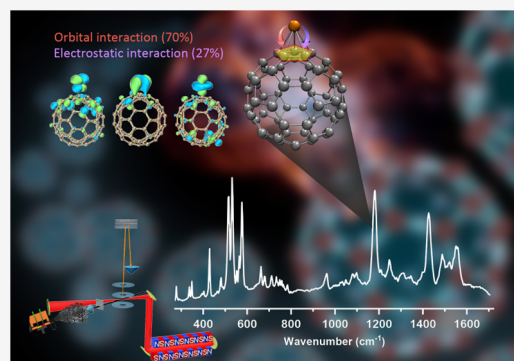
ACCESS |

Metrics & More

Article Recommendations

Supporting Information

**ABSTRACT:** Buckminsterfullerene  $C_{60}$  has received extensive research interest since its discovery. In addition to its interesting intrinsic properties of exceptional stability and electron-accepting ability, the broad chemical tunability by decoration or substitution on the  $C_{60}$ -fullerene surface makes it a fascinating molecule. However, to date, there is uncertainty about the binding location of such decorations on the  $C_{60}$  surface, even for a single adsorbed metal atom. In this work, we report the gas-phase synthesis of the  $C_{60}V^+$  complex and its in situ characterization by mass spectrometry and infrared spectroscopy with the help of quantum chemical calculations and molecular dynamics simulations. We identify the most probable binding position of a vanadium cation on  $C_{60}$  above a pentagon center in an  $\eta^5$ -fashion, demonstrate a high thermal stability for this complex, and explore the bonding nature between  $C_{60}$  and the vanadium cation, revealing that large orbital and electrostatic interactions lie at the origin of the stability of the  $\eta^5\text{-}C_{60}V^+$  complex.



## INTRODUCTION

$C_{60}$  was discovered by Smalley, Kroto, Curl, and co-workers in the mid-1980s and was recognized as the third allotrope of carbon besides graphite and diamond.<sup>1,2</sup> Its discovery has opened the age of fullerene science and sparked worldwide interest, demonstrated by the awarding of the Nobel Prize in Chemistry in 1996. This football-shaped molecule, consisting of 20 hexagons and 12 pentagons with icosahedral ( $I_h$ ) symmetry, has interesting intrinsic properties of high stability and electron-accepting ability. In addition, fullerenes show broad structural tunability by decoration or substitution, either on their exterior surface or interior cavity, making them exceptional materials to explore.<sup>2,3</sup> In particular, significant interest in metal-doped fullerenes has emerged just a few years after the discovery of  $C_{60}$ . For instance, alkali metal-doped fullerene films were found to present superconducting behavior,<sup>4</sup> alkali and alkaline earth metal-doped fullerenes have high hydrogen storage capability,<sup>5,6</sup> transition metal-doped fullerenes show interesting applications in organic photovoltaic cells,<sup>7,8</sup> and hybrid structures of  $C_{60}$ -fullerene with coinage metals can be used in novel nanoscale devices.<sup>9,10</sup> Each of these phenomena is to some extent linked to electron transportation in hybrid fullerene–metal junctions.<sup>7,10–13</sup>

However, there is to date little experimental benchmarking data on the preferred metal binding sites, which is essential to understand the character of the metal-fullerene bonds, which in turn allows better understanding and/or improving the design of fullerene-based functional materials. Surprisingly, even for a single metal atom, there is no unambiguous experimental evidence regarding its binding site and

interaction nature with the  $C_{60}$  surface.<sup>13</sup> For example, employing X-ray and ultraviolet photoelectron spectroscopy, Kröger et al. showed that the nature of the interaction between Au and  $C_{60}$  is covalent, but no signature of charge transfer was found in their study.<sup>14</sup> Lyon and Andrews concluded, based on matrix isolation infrared spectroscopy, that the Au atom preferentially binds on the pentagonal ring of  $C_{60}$  and also pointed out that their conclusion may be subject to a matrix effect.<sup>15</sup> In contrast, the vertex binding site ( $\eta^1$ ) has been found to be most stable for  $C_{60}\text{Au}_1$  from DFT calculations including spin-orbit coupling.<sup>16,17</sup> A third possible Au binding site was obtained in the work of Shukla et al., who found the bridge site when  $C_{60}$  is sandwiched between two Au clusters.<sup>11</sup> Although the bonding scheme in sandwich-type complexes may be different from that in  $C_{60}$  complexes with single metal atoms, these examples illustrate the challenge in achieving firm conclusions on the binding sites of metal atoms or clusters on the  $C_{60}$  surface and thus their bonding nature. Using “indirect” structural information based on mass spectrometry, Kaya and co-workers suggested that the vanadium cation ( $V^+$ ) binds above the hexagonal ring of  $C_{60}$ <sup>18</sup> as predicted by several

Received: August 7, 2023

Published: September 27, 2023



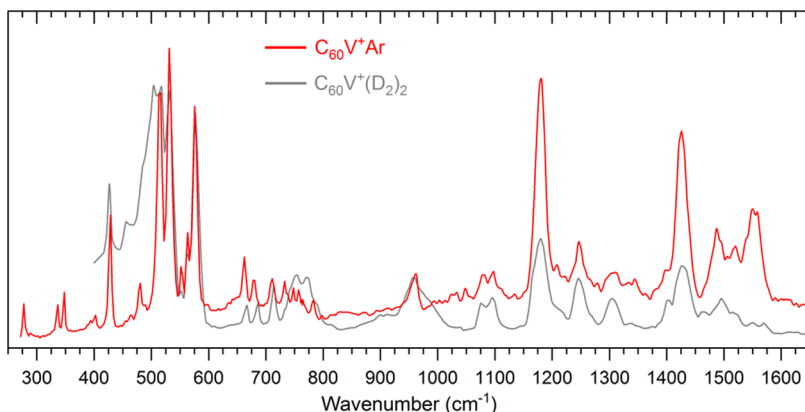


**Figure 1.** IRMPD spectrum of Ar-tagged  $C_{60}V^+$  in the 250–1700  $\text{cm}^{-1}$  range (red). The spectrum of  $D_2$ -tagged  $C_{60}V^+$  with two tagging  $D_2$  molecules in 400–1700  $\text{cm}^{-1}$  range (gray) is replotted from ref 23 for comparison.

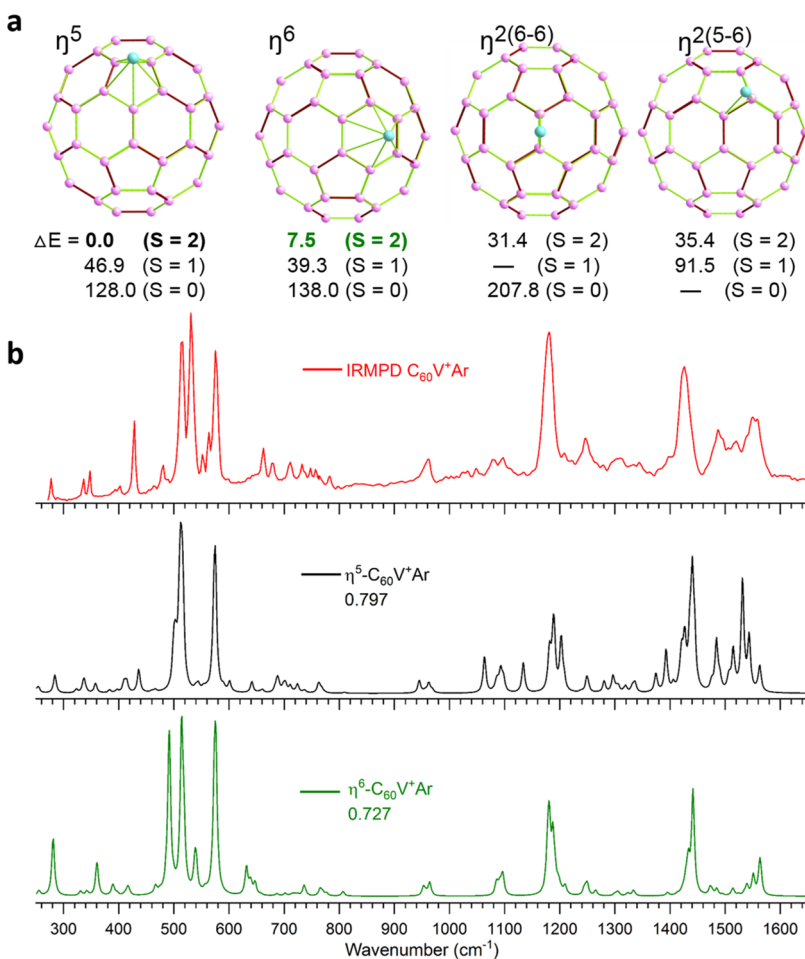


**Figure 2.** Experimental infrared spectrum of  $C_{60}V^+\text{Ar}$  and its comparison with theoretical calculations. (a) Four optimized structures, i.e.,  $\eta^5$ ,  $\eta^6$ ,  $\eta^2(6-6)$ , and  $\eta^2(5-6)$ , and their relative stabilities ( $\Delta E$ , in  $\text{kJ/mol}$ ) at the BPW91/6-31G(d) level. (b) Comparison of the experimental spectrum with simulated ones (broadened using Lorentzian line shapes of 6  $\text{cm}^{-1}$  full width at half-maximum) for the lowest-energy spin states ( $S = 2$ ) in  $\eta^5$  and  $\eta^6$  configurations at the BPW91/6-31G(d) level of theory. The cosine similarity scores are indicated for the simulated spectra.

density functional theory (DFT) calculations,<sup>13,19</sup> but in this case, conclusive evidence is missing as well.

Recently, we have developed an experimental protocol to measure the infrared spectra of  $[C_{60}\text{-Metal}]^+$  complexes via messenger-tagged infrared multiple photon dissociation (IRMPD) spectroscopy.<sup>20–23</sup> These fundamental experimental studies have an impact in multiple fields, including catalysis

and astrophysics. We showed that a single vanadium cation supported on  $C_{60}$  can efficiently catalyze the water splitting process to produce  $H_2$  upon infrared light absorption, demonstrating the importance of carbonaceous supports in single-atom catalysts,<sup>20,21</sup> and proposed that the complexes of fullerene with cosmic abundant metals such as iron can be promising carriers of astronomical unidentified infrared

bands.<sup>23</sup> However, fundamental questions regarding the exact binding site and detailed interaction nature of the metal with C<sub>60</sub> remain to be answered. In this work, we conclude from our combined IRMPD spectroscopy and comprehensive theoretical calculations that the most probable location of V<sup>+</sup> on C<sub>60</sub> is above the pentagon. We also explore the bonding nature and origin of the stability of the fullerene–metal complex.

## RESULTS AND DISCUSSION

The laboratory infrared spectrum of the gas-phase C<sub>60</sub>V<sup>+</sup> complex was measured via IRMPD spectroscopy using the intense far- to mid-infrared light from the Free Electron Laser for Intra-Cavity Experiments (FELICE).<sup>24</sup> Recently, we reported the IRMPD spectrum of C<sub>60</sub>V<sup>+</sup> using D<sub>2</sub> as a messenger in the spectral range of 400–1600 cm<sup>-1</sup> (see details in the Methods section),<sup>23</sup> but the presence of D<sub>2</sub> molecules leads to spectral features containing effects from the D<sub>2</sub> tagging with several small features around 500 and 750 cm<sup>-1</sup> due to D<sub>2</sub> motion.

To obtain higher-quality IRMPD spectra of C<sub>60</sub>V<sup>+</sup>, we synthesized Ar-tagged C<sub>60</sub>V<sup>+</sup> complexes. The calculated Ar–C<sub>60</sub>V<sup>+</sup> binding energy of only 3.6 kJ/mol is much lower than the D<sub>2</sub>–C<sub>60</sub>V<sup>+</sup> binding energy of 30.5 kJ/mol. A lower messenger binding energy means it has less influence on both the geometric and electronic properties of the parent species (Figures S1–S3).<sup>25</sup> Simultaneously, the photon energy of 300 cm<sup>-1</sup> light is about 3.6 kJ/mol, implying that fragmentation of the Ar-tagged C<sub>60</sub>V<sup>+</sup> complex can occur by absorbing a single photon above 300 cm<sup>-1</sup> (see molecular dynamics simulations below). Therefore, the IRMPD spectrum of the Ar-tagged C<sub>60</sub>V<sup>+</sup> complex should be close to a linear absorption spectrum.

Figure 1 shows the infrared spectrum of Ar-tagged C<sub>60</sub>V<sup>+</sup>, and for comparison, the D<sub>2</sub>-tagged C<sub>60</sub>V<sup>+</sup> with two tagging D<sub>2</sub> molecules is replotted from ref 23 as well. The comparison, on the one hand, shows that the infrared spectrum using an Ar tag has a higher spectral resolution as seen by the sharper features, presumably because fewer photons must be absorbed to fragment this complex compared to the D<sub>2</sub>-tagged C<sub>60</sub>V<sup>+</sup>. On the other hand, Figure 1 shows that the two spectra are almost identical if disregarding the peak intensities and specific features in the 400–500 cm<sup>-1</sup> range and around 750 cm<sup>-1</sup>, verifying our previously assigned effect of the D<sub>2</sub> tag on the vibrational spectrum of C<sub>60</sub>V<sup>+</sup>.<sup>23</sup> In addition, there are several new bands below 400 cm<sup>-1</sup>, which could be characteristic of the C<sub>60</sub>–metal interactions (see Figures S4 and S5).

To extract information about the vanadium binding site, we first carried out quantum chemical calculations to obtain candidate structures of the C<sub>60</sub>V<sup>+</sup> complex. Because of the I<sub>h</sub> symmetry of C<sub>60</sub>, only five different binding sites, i.e., η<sup>6</sup>, η<sup>5</sup>, η<sup>2(6-6)</sup>, η<sup>2(5-6)</sup>, and η<sup>1</sup>, need to be considered.<sup>20</sup> In those structures, the V atom binds with a hexagonal center, a pentagonal center, a bridge of two hexagons, a bridge of a hexagon and a pentagon, and atop of a C atom, respectively. Since the ground state of V<sup>+</sup> is [Ar]3d<sup>3</sup>4s<sup>1</sup>, the interaction of V<sup>+</sup> with the closed-shell molecule C<sub>60</sub> to form C<sub>60</sub>V<sup>+</sup> could result in S = 2, 1, and 0 spin states, which all have been considered.

In Figure 2a, four optimized structures of C<sub>60</sub>V<sup>+</sup>, including η<sup>5</sup>, η<sup>6</sup>, η<sup>2(6-6)</sup>, and η<sup>2(5-6)</sup>, at the BPW91/6-31G(d) level, together with their relative stabilities, are presented. The η<sup>1</sup> structure was unstable in the calculations and converged to either η<sup>5</sup> or η<sup>6</sup>, and the calculations show that the high-spin

states have much higher stabilities, by over 30 kJ/mol, than those of the low-spin states. Based on energetics, the two bridge structures, η<sup>2(6-6)</sup> and η<sup>2(5-6)</sup>, can be ruled out as they are much higher in energy than the most stable η<sup>5</sup> structure by more than 30 kJ/mol. However, given that the typical accuracies of DFT methods are not better than 10 kJ/mol, the current energy difference between the η<sup>5</sup> and η<sup>6</sup> structures is insufficient to rule out either one, in addition to the possibility that higher-energy isomers might be kinetically trapped due to large barriers (see below). Hence, both structures could coexist in the experiment. One could argue that the current bias toward the η<sup>5</sup> structure of 7.8 kJ/mol (Gibbs free energy at 300 K) lower in energy, which increases to 10.6 kJ/mol when going to the larger def2-TZVP basis set, strengthens the case for the pentagon, but these arguments remain tentative, if only because full thermalization in the experiment cannot be assumed.

Given the above energetics, a comparison of the experimental spectrum with the simulated ones is shown only for the η<sup>5</sup> or η<sup>6</sup> structures in S = 2 spin states in Figure 2b (a comparison with other isomers is presented in Figure S6). However, solely from a visual inspection, it is difficult to make a conclusive assignment of the experimental spectrum to any of the structures alone. For example, in the 900–1600 cm<sup>-1</sup> range, the match with η<sup>6</sup> appears quite good, apart from a missing band just below 1500 cm<sup>-1</sup>. However, below 800 cm<sup>-1</sup>, there are more discrepancies, e.g., a few spectral features around 700 cm<sup>-1</sup>, a relatively intense band at 630 cm<sup>-1</sup>, and a clear mismatch below 450 cm<sup>-1</sup>. In turn, the lowest-energy η<sup>5</sup> structure overall does quite well but fails to accurately predict the splitting of the 510–530 cm<sup>-1</sup> experimental band with a small frequency difference (see the vibrational vectors at 500 and 512 cm<sup>-1</sup> in Figure S4) in the predicted double-peak feature. Additionally, the relatively strong sharp experimental features below 500 cm<sup>-1</sup> (see close-up in the 250–650 cm<sup>-1</sup> spectral range in Figure S5 and the related vibrational mode vectors in Figure S4), computationally identified as motions directly involving the V–C<sub>60</sub> bond, do not allow for an unambiguous assignment.

Consequently, other analytical methods must be considered. A useful tool to address this problem is the cosine similarity test.<sup>26</sup> This test, as detailed in the Methods section, was developed as a quantitative measure to evaluate the similarity between two curves. It has been successfully employed as an objective metric to evaluate the agreement between calculated and experimental infrared spectra.<sup>27,28</sup> The calculated cosine similarity scores are provided in Figures 2b and S6; the η<sup>5</sup> structure has the highest score among the four Ar-tagged structural isomers. We tested the application of uniform scaling factors for the calculated harmonic frequencies, and the same trend for the calculated cosine similarity scores is obtained. While the value of 0.797 (a value of 1 should be obtained for identical spectra) reflects some disagreement between DFT calculations and experiments as illustrated in the previous section, it is about 0.07 larger than the value of 0.727 for η<sup>6</sup> C<sub>60</sub>V<sup>+</sup>. According to previous studies,<sup>26–28</sup> such difference allows to differentiate the η<sup>5</sup> structure from the η<sup>6</sup> structure, making the quantitative cosine similarity analysis objectively favoring the assignment of the experimental spectrum to η<sup>5</sup> C<sub>60</sub>V<sup>+</sup>.

From the above energetic stability and spectral comparison analysis, we conclude that η<sup>5</sup> C<sub>60</sub>V<sup>+</sup> is the structure existing in our experiment. This contrasts with previous theoretical

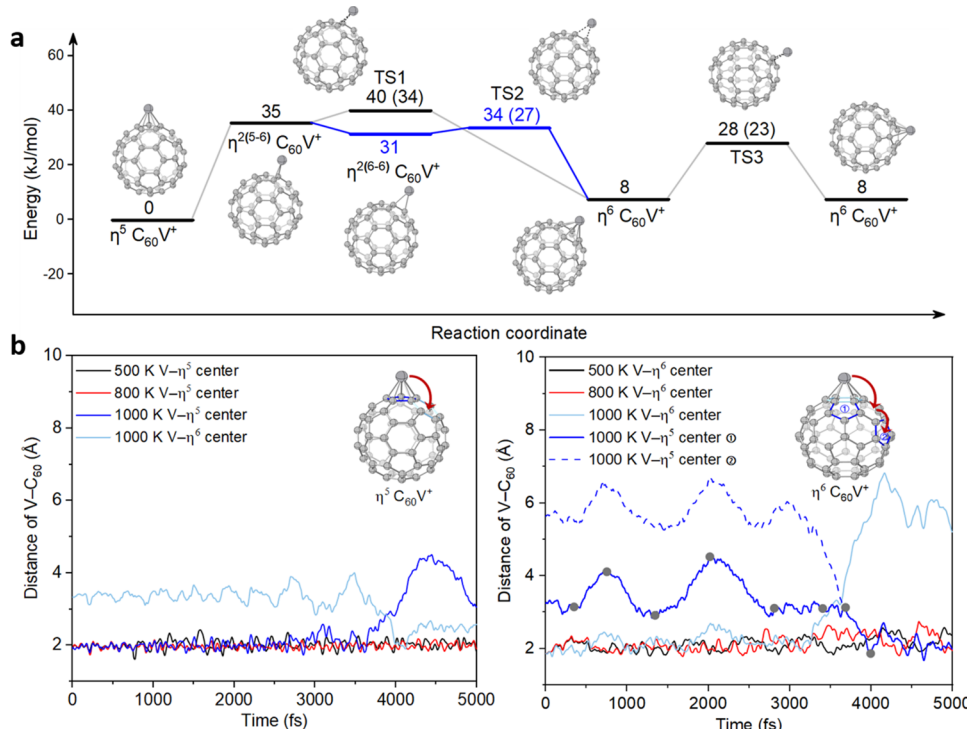


**Figure 3.** (a) Isomerization pathways linking the four  $C_{60}V^+$  isomers calculated at the BPW91/6-31G(d) level with all structures shown with a similar view. Two different pathways connecting the interconversion between  $\eta^5$  and  $\eta^6 C_{60}V^+$  are colored black and blue, respectively. For transition states, the energies without ZPE correction are also presented in parentheses. (b) Distances between V and the center of the pentagon and hexagon of  $C_{60}$  in 5 ps BOMD simulations at 500, 800, and 1000 K in  $\eta^5 C_{60}V^+$  (left) and  $\eta^6 C_{60}V^+$  (right), respectively. Red arrows are utilized to guide the eye toward the conversion pathway during the simulation. In the right panel, the distances between V and the center of the closest pentagon (center<sup>(1)</sup>) and the finally resultant pentagon (center<sup>(2)</sup>) in the simulation are shown, respectively, in solid and dashed lines. Snapshots indicated with gray circles are provided in Figure S7 to show the location changes of V during BOMD simulations.

predictions from Sankar De et al.<sup>13</sup> and Robledo et al.<sup>19</sup> that the  $\eta^6$  structure is most stable. Sankar De et al. employed the VASP program to optimize the different isomers of  $C_{60}V$  and calculate their stabilities, but this method cannot describe the exact atomic configuration of V. The B3LYP functional used by Robledo et al. gives, according to our systematic calculations in Table S1, an almost degenerate stability for  $\eta^5$  and  $\eta^6 C_{60}V^+$  with the  $\eta^5$  structure being only 0.9 kJ/mol more stable. Such a small energy difference does not allow a meaningful conclusion about the relative stability because the typical accuracies of DFT methods are not better than 10 kJ/mol.

In addition, Nagao et al. employed the 18-electron counting rule to explain the number of CO molecules that can bind with  $C_{60}V^+$  in their mass spectrometric study, which suggests that  $V^+$  binds with a hexagon of  $C_{60}$  in a  $\eta^6$  configuration.<sup>18</sup> That empirical interpretation does not allow one to draw a solid conclusion, emphasizing the critical importance of spectroscopic data. It should be noted that the calculated infrared spectra of  $C_{60}V^+$  with and without Ar tag show essentially no difference as supported by the detailed comparison and calculated cosine similarity scores well above 0.9 (Figure S1). The minor effect of the Ar tag on the structure of  $C_{60}V^+$  has been verified by calculating the root-mean-square deviation (RMSD) values below 0.01 Å between the  $C_{60}V^+$  and  $C_{60}V^+Ar$  geometries (Figure S2).

In the following, we seek to assess the thermal stability of  $C_{60}V^+$  by exploring the isomerization pathways of its four isomers using both quantum chemical calculations and Born–Oppenheimer molecular dynamics (BOMD) simulations as

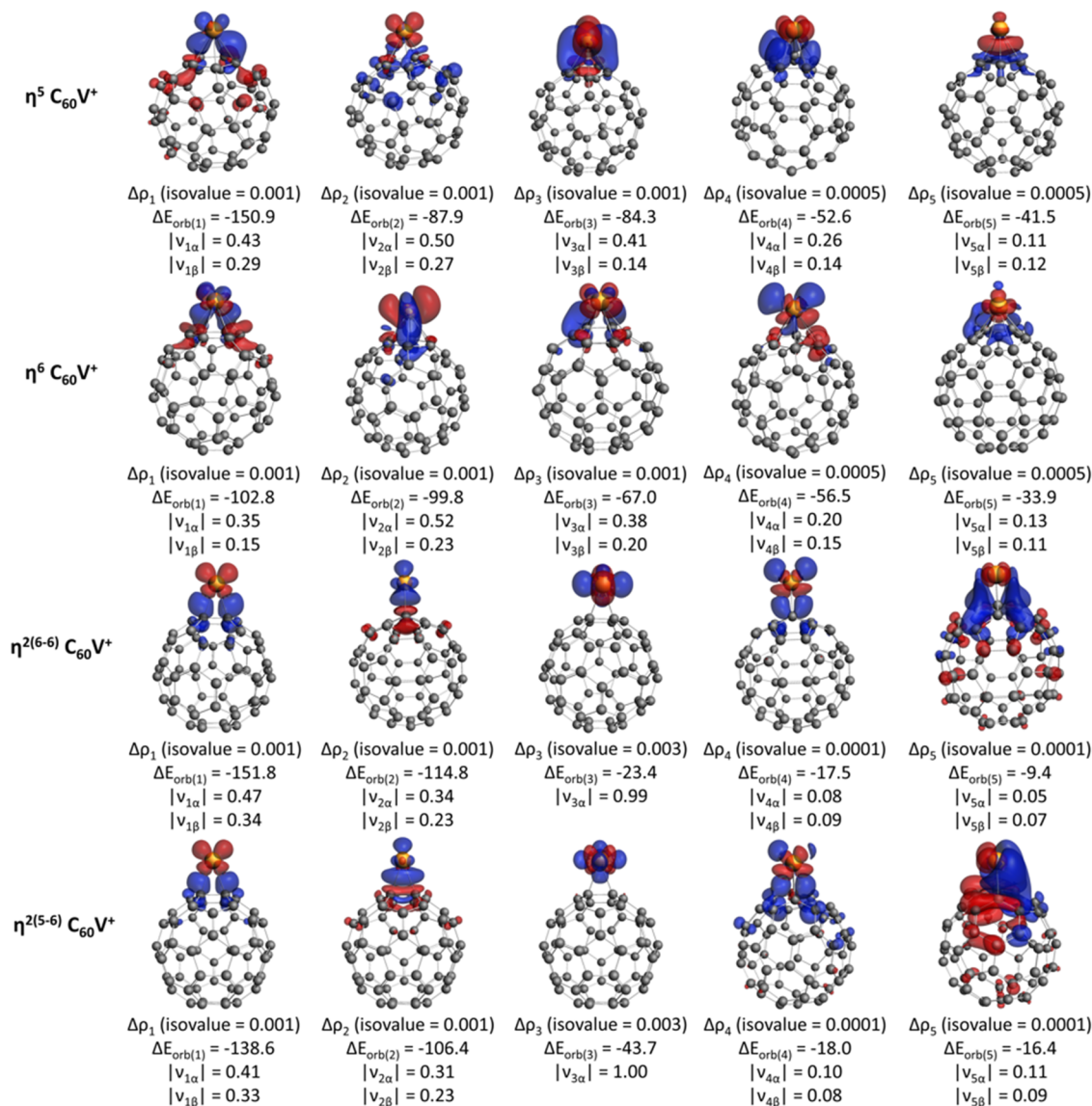
well as the bonding nature by conducting energy decomposition analysis (EDA). Figure 3a presents the isomerization pathways of the four  $C_{60}V^+$  isomers calculated at the BPW91/6-31G(d) level of theory. It can be seen that interconversion barriers are relatively large, although not completely insurmountable. The calculated pathways show that the interconversion between  $\eta^5$  and  $\eta^6 C_{60}V^+$  can either go directly through  $\eta^{2(5-6)}$  (black) or via both  $\eta^{2(5-6)}$  and  $\eta^{2(6-6)}$  (blue). Note that the isomerization between two bridge-site isomers, i.e.,  $\eta^{2(5-6)}$  and  $\eta^{2(6-6)}$ , should be via a  $\eta^1$  structure; unfortunately, the transition state structure could not be located, implying that it might be a barrierless process.

Figure 3b shows the change of the V–C<sub>60</sub> distances in BOMD simulations of 5 ps at 500, 800, and 1000 K for both  $\eta^5 C_{60}V^+$  (left panel) and  $\eta^6 C_{60}V^+$  (right panel). At low temperatures of 500 and 800 K, the V–C<sub>60</sub> distances do not change significantly for both isomers, indicating no interconversion between the different isomers of  $C_{60}V^+$ . This is consistent with the relatively large interconversion barriers of around 30 kJ/mol between different isomers starting from either  $\eta^5$  or  $\eta^6 C_{60}V^+$ . However, at an elevated temperature, the internal energy of  $C_{60}V^+$  increases and its thermal motion makes it possible for the  $V^+$  to reach the different binding sites. For both  $\eta^5$  and  $\eta^6 C_{60}V^+$  isomers without an Ar tag, the simulations show that both V– $\eta^5$  and V– $\eta^6 C_{60}V^+$  distances suddenly increase significantly around 3.5 ps at 1000 K, while when tagging with Ar, a significant increase in the V– $\eta^6 C_{60}V^+$  center distance is already observed at 800 K for the  $\eta^6$  isomer. This distance remains relatively constant for the  $\eta^5$  isomer during the 5 ps simulation time at 800 K (see Figure S8 that

**Table 1.** Bond Dissociation Energies ( $D_0$ )<sup>a</sup> and Results from Energy Decomposition Analysis (EDA-NOCV)<sup>b</sup> for Four  $C_{60}V^+$  Isomers<sup>c</sup>

|  | $\eta^5 C_{60}V^+$                                  | $\eta^6 C_{60}V^+$                                  | $\eta^{2(6-6)} C_{60}V^+$                       | $\eta^{2(5-6)} C_{60}V^+$                       |
|--|---|---|---|---|
| $D_0$                                      | -264.3  | -261.1  | -238.1  | -234.3  |
| $\Delta E_{\text{int}}$                    | -266.9  | -258.8  | -259.7  | -260.8  |
| $\Delta E_{\text{pauli}}$                  | 472.1   | 446.6   | 331.1   | 317.7   |
| $\Delta E_{\text{disp}}$ <sup>d</sup>      | -25.4 (3.4%)  | -25.3 (3.6%)  | -31.7 (5.4%)                                    | -30.5 (5.3%)                                    |
| $\Delta E_{\text{elstat}}$ <sup>d</sup>    | -199.4 (27.0%)                                      | -193.5 (27.4%)                                      | -181.0 (30.6%)                                  | -164.2 (28.4%)                                  |
| $\Delta E_{\text{orb}}$ <sup>d</sup>       | -514.2 (69.6%)                                      | -486.6 (69.0%)                                      | -378.1 (64.0%)                                  | -383.8 (66.3%)                                  |
| $\Delta E_{\text{orb}(1)}$ <sup>e</sup>    | -150.9 (29.3%) $V^+(d_{zx}) \leftarrow C_{60}$      | -102.8 (21.1%) $V^+(d_{zx}) \leftarrow C_{60}$      | -151.8 (40.1%) $V^+(d_{zx}) \rightarrow C_{60}$ | -138.6 (36.1%) $V^+(d_{zx}) \rightarrow C_{60}$ |
| $\Delta E_{\text{orb}(2)}$ <sup>e</sup>    | -87.9 (17.1%) $V^+(d_{yz}) \rightarrow C_{60}$      | -99.8 (20.5%) $V^+(d_{x^2-y^2}) \rightarrow C_{60}$ | -114.8 (30.4%) $V^+(d_{z^2}) \leftarrow C_{60}$ | -106.4 (27.7%) $V^+(d_{z^2}) \leftarrow C_{60}$ |
| $\Delta E_{\text{orb}(3)}$ <sup>e</sup>    | -84.3 (16.4%) $V^+(d_{x^2-y^2}) \rightarrow C_{60}$ | -67.0 (13.8%) $V^+(d_{xy}) \rightarrow C_{60}$      | -23.4 (6.2%) $V^+$ polarization                 | -43.7 (11.4%) $V^+$ polarization                |
| $\Delta E_{\text{orb}(4)}$ <sup>e</sup>    | -52.6 (10.2%) $V^+(d_{xy}) \rightarrow C_{60}$      | -56.5 (11.6%) $V^+(d_{yz}) \rightarrow C_{60}$      | -17.5 (4.6%) $V^+(d_{yz}) \rightarrow C_{60}$   | -18.0 (4.7%) $V^+(d_{yz}) \rightarrow C_{60}$   |
| $\Delta E_{\text{orb}(5)}$ <sup>e</sup>    | -41.5 (8.1%) $V^+(d_z) \rightarrow C_{60}$          | -33.9 (7.0%) $V^+(d_z) \rightarrow C_{60}$          | -9.4 (2.5%) $V^+(d_{xy}) \rightarrow C_{60}$    | -16.4 (4.3%) $V^+(d_{xy}) \rightarrow C_{60}$   |
| $\Delta E_{\text{orb(rest)}}$ <sup>e</sup> | -97.0 (18.9%)                                       | -126.6 (26.0%)                                      | -61.2 (16.2%)                                   | -60.7 (15.8%)                                   |

<sup>a</sup>Values calculated at the BPW91/6-31G(d) level. <sup>b</sup>Values calculated at the BP86-D3(BJ)/TZ2P//BPW91/6-31G(d) level using  $V^+$  (quintet) and  $C_{60}$  (singlet) as interacting fragments. <sup>c</sup>All energies are in kJ/mol. <sup>d</sup>Values in parentheses are the relative contributions to the total attractive interactions  $\Delta E_{\text{disp}} + \Delta E_{\text{elstat}} + \Delta E_{\text{orb}}$ . <sup>e</sup>Values in parentheses are the relative contributions to  $\Delta E_{\text{orb}}$ .

**Figure 4.** Plots of the deformation densities  $\Delta\rho_1$  to  $\Delta\rho_5$  associated with the pairwise interactions  $\Delta E_{\text{orb}(1)}$  to  $\Delta E_{\text{orb}(5)}$  in  $C_{60}V^+$  with corresponding energies (kJ/mol) and eigenvalues ( $v$ ) by using  $V^+$  (quintet) and  $C_{60}$  (singlet) as interacting fragments. The charge flow is colored red to blue.

also includes the change of V–Ar distances in Ar-tagged  $C_{60}V^+$  structures). The interconversion starting from  $\eta^6 C_{60}V^+$  is complicated, as it first starts converting to another  $\eta^6 C_{60}V^+$  at about 3.5 ps and then to  $\eta^5 C_{60}V^+$  at around 4.0 ps at a temperature of 1000 K (Figure 3b, right), consistent with the calculated isomerization pathways (Figure 3a). It then maintains the  $\eta^5 C_{60}V^+$  structure for the remaining simulation time, implying the slightly higher stability of  $\eta^5 C_{60}V^+$  compared to that of  $\eta^6 C_{60}V^+$ . Besides, the simulations show that the Ar tag gets detached from  $C_{60}V^+$  in the temperature range of 500–800 K for both  $\eta^5$  and  $\eta^6 C_{60}V^+$  (Figure S8), in agreement with their low Ar– $C_{60}V^+$  binding energies of only 3–4 kJ/mol from DFT calculations.

To obtain a more direct view of the interconversion of the four  $C_{60}V^+$  isomers, we further increased the simulation temperature to 2000 K, assuming that  $C_{60}V^+$  may freely access its different isomers at such a high temperature. In Figure S9, we plotted the statistical trajectories of  $C_{60}V^+$  in different isomers from a 5 ps BOMD simulation at 2000 K with  $\eta^5 C_{60}V^+$  as the starting point. It can be seen that the four isomers indeed can convert to each other, and we summed the total time that each isomer stays to be 27, 24, 34, and 15% for  $\eta^5$ ,  $\eta^6$ ,  $\eta^{2(5-6)}$ , and  $\eta^{2(6-6)}$ , respectively. Ideally, such values could represent the isomeric populations during the simulation and reflect the relative stability of the isomers. However, 5 ps simulation time may not be long enough to allow the four isomers to achieve a statistical thermodynamic equilibrium, under which condition, the population of the isomers would follow a Boltzmann distribution depending on their thermodynamic stability. Movies showing the trajectories of the BOMD simulations are provided in the Supporting Information.

The bonding nature between  $V^+$  and  $C_{60}$  is investigated using energy decomposition analysis combined with natural orbitals for chemical valence (EDA-NOCV) at the BP86-D3(BJ)/TZ2P level for all of the four  $C_{60}V^+$  isomers optimized at the BPW91/6-31G(d) level.<sup>29</sup> Table 1 summarizes the calculated results for the interactions between the  $V^+$  (quintet) and  $C_{60}$  (singlet) fragments. The calculated interaction energies  $\Delta E_{\text{int}}$  are in good agreement with the calculated bond dissociation energies ( $D_0$ ). The main contributions to the total bonding interactions  $\Delta E_{\text{int}}$  come from the electrostatic term  $\Delta E_{\text{elstat}}$  and the orbital interaction term  $\Delta E_{\text{orb}}$ . In particular, both  $\Delta E_{\text{orb}}$  and  $\Delta E_{\text{elstat}}$  have the highest absolute values for  $\eta^5 C_{60}V^+$ . The larger bonding interactions of  $\eta^5 C_{60}V^+$  compared to those of the other three isomers are consistent with the higher stability of  $\eta^5 C_{60}V^+$  found at the BPW91/6-31G(d) level. Further decomposition of the total orbital interactions  $\Delta E_{\text{orb}}$  results in the individual orbital terms including  $\Delta E_{\text{orb}(1)} - \Delta E_{\text{orb}(5)}$ , corresponding to the five d orbitals of V. This decomposition analysis shows subtle changes of the orbital orders among the four isomers, suggesting a different bonding scenario.

The effect of orbital interactions on the charge distribution can be seen from the shape of the deformation densities ( $\Delta\rho$ ) associated with the orbital interactions. Figure 4 shows the contour plots of the deformation densities  $\Delta\rho_{(1)}$  to  $\Delta\rho_{(5)}$  that are connected to pairwise interactions  $\Delta E_{\text{orb}(1)}$  to  $\Delta E_{\text{orb}(5)}$  in  $C_{60}V^+$  (Table 1). Among these components, charge transfer (donor–acceptor interactions between the two fragments) and polarization (unoccupied–occupied orbital mixing on  $V^+$  due to the presence of  $C_{60}$ ) are dominant contributions. In the case of  $\eta^5 C_{60}V^+$ , two different bond types are revealed. First, the dative bond ( $\Delta\rho_{(1)}$ ) is constructed by donation from the

highest occupied molecular orbital (HOMO) of  $C_{60}$  to the  $V^+$   $d_{zx}$  orbital, which contributes most to the total orbital interactions. Second,  $\Delta\rho_{(2)} - \Delta\rho_{(5)}$  of  $\eta^5 C_{60}V^+$  corresponds to the dative bond constructed by the donation from  $d_{yz}$ ,  $d_{x^2-y^2}$ ,  $d_{xy}$ , and  $d_{z^2}$  of  $V^+$  to the lowest unoccupied molecular orbital (LUMO) of  $C_{60}$ , thus forming the four singly occupied orbitals of  $C_{60}V^+$ . The analysis suggests that orbital interactions play a crucial role in charge transfer between  $V^+$  and  $C_{60}$ . It is similar for the other three isomers, but delicate differences exist regarding the orbital energy orders and thus the electronic structures. Such delicate differences could lead to subtle variations in the functionality of decorated fullerenes and would cause  $C_{60}$ -metal complexes to have unique spectral signatures in the ultraviolet and optical wavelength region. That may potentially be important to investigate their relevance to the astronomical mysterious diffuse interstellar bands.<sup>23,30,31</sup>

## CONCLUSIONS

In summary, we investigated the binding position of a single  $V^+$  on the buckyball surface by combining Ar tagging infrared spectroscopy, quantum chemical calculations, and molecular dynamics simulations. Comparison between the experimental and calculated infrared spectra with the aid of an objective similarity analysis suggests that Ar tagging has a negligible effect on both the geometric and vibrational structures of  $C_{60}V^+$  and that the most probable binding site for  $V^+$  is the center of a  $C_{60}$  pentagon ( $\eta^5$  binding). Calculated isomerization pathways and Born–Oppenheimer molecular dynamics simulations at a range of temperatures further show a high thermal stability of  $C_{60}V^+$  beyond temperatures of 800 K. Chemical bonding analysis reveals that the large orbital and electrostatic interactions are responsible for the high stability of  $C_{60}V^+$ , in particular for the  $\eta^5$  structure. This information is of critical importance for the rational design of fullerene-based functional materials.

## METHODS

**Experimental Section.** The  $C_{60}V^+$  complex is synthesized in vacuum by a dual-target dual-laser ablation source, which is a modified version of the Smalley-type laser vaporization source used in the discovery of  $C_{60}$  in 1985 (ref 1). Our cluster source has been described in detail previously.<sup>32</sup> For the synthesis of  $C_{60}V^+$ , we use a bulk vanadium target and a fullerene target that is obtained by cold-pressing  $C_{60}$  powder.<sup>20–23,33</sup> Both targets are vaporized by 532 nm laser pulses from two independent Nd:YAG lasers, both operated at 10 Hz repetition rates. Note that the laser for the fullerene target is off-focused on the fullerene target and is operated with a much lower power compared to the laser for the vanadium target to avoid fragmentation of the fullerenes. The vaporized neutral  $C_{60}$  molecules and metal plasma, containing metal cations, collide with each other in the presence of He gas, introduced through a pulsed valve with a 6 bar stagnation pressure, which triggers the formation and cooling of the complexes. We assume  $[C_{60}\text{-Metal}]^+$  complexes to be thermalized to room temperature before expansion into a vacuum, moderately cooling their internal degrees of freedom.

The high stability of  $C_{60}V^+$ , characterized by a calculated binding energy of 2.82 eV at BPW91/6-31G(d) (see below) between  $C_{60}$  and  $V^+$ , precludes the recording of high-quality infrared spectrum due to the inefficient dissociation induced by the infrared photon absorption as shown in our recent work.<sup>23</sup> Hence, the messenger tagging technique must be utilized, which has been well established in the past decades to obtain the vibrational or electronic spectra of molecular species via photodissociation.<sup>30,34,35</sup> Previously, we employed  $D_2$  as the tag for  $C_{60}V^+$ , but the calculated binding energy of  $D_2$  with  $C_{60}V^+$

is about 30.5 kJ/mol. In this work, we utilize Ar, which, with a calculated binding energy of about 3.6 kJ/mol, corresponding to only one photon at 300 cm<sup>-1</sup>, is a more sensitive messenger and simultaneously, through its weaker interaction, will lead to fewer changes to the intrinsic vibrational structure of the parent species. The Ar-tagged C<sub>60</sub>V<sup>+</sup> complex was formed by seeding about 2% Ar into a He carrier gas. After expansion into vacuum through a conical nozzle, the cluster beam is formed and shaped by a 2 mm diameter skimmer and a 2 mm slit aperture, before entering the extraction zone of a perpendicular reflectron time-of-flight (TOF) mass spectrometer.

IRMPD experiments are performed by overlapping the shaped cluster beam with IR light of the Free Electron Laser for Intra-Cavity Experiments FELICE.<sup>24</sup> The measurements were conducted with two FEL settings, covering the 250–750 and 600–1800 cm<sup>-1</sup> spectral ranges, at a repetition rate of 5 Hz. This allowed us to alternatingly record mass spectra with and without IR laser interaction. Laser excitation in resonance with a vibrational mode heats up the clusters by infrared photon absorption and intramolecular vibrational redistribution (IVR). When the internal energy of the cluster is high enough, fragmentation (dissociation) takes place on the time scale of the experiment via the lowest-energy fragmentation channel, in the current case desorption of Ar from C<sub>60</sub>V<sup>+</sup>Ar. Here, the Ar atom serves as noninterfering weakly bound messenger that will be shed if IR radiation is resonantly absorbed, representing a sensitive probe by mass spectrometry. Care has been taken with the FEL light focusing to minimize saturation effects and to avoid the destruction of the C<sub>60</sub> cage, which is confirmed by the absence of C<sub>60-2m</sub><sup>+</sup> fragments in the mass spectra. In the current experiment, the absorption of one infrared photon might be enough to induce fragmentation due to the weak Ar–C<sub>60</sub>V<sup>+</sup> interaction, making the experiment likely to be IRPD.

The FEL was scanned in wavenumber steps of 3 cm<sup>-1</sup>, and the IR wavelength was calibrated using a grating spectrometer. The experiments allow IR spectra to be obtained by comparing the mass spectrometric intensities of C<sub>60</sub>V<sup>+</sup> and its Ar-tagged complex with [I( $\nu$ )] and without ( $I_0$ ) FEL light irradiation. We first calculate the branching ratio  $B$  of the number of C<sub>60</sub>V<sup>+</sup>Ar<sub>1</sub> ions to all C<sub>60</sub>V<sup>+</sup>Ar<sub>0,1</sub> ions,

$$B = I[\text{C}_{60}\text{V}^+\text{Ar}_1] / \sum I[\text{C}_{60}\text{V}^+\text{Ar}_{0,1}] \quad (1)$$

Under the assumption of a constant Ar adsorption rate, this eliminates fluctuations in the metal-fullerene synthesis. We then calculate the depletion  $D(\nu)$  as a function of IR frequency  $\nu$  by taking the natural logarithmic ratio of the branching ratios with and without IR irradiation

$$D(\nu) = -\ln[B(\nu)/B_0] \quad (2)$$

The depletion  $D(\nu)$  is divided by the laser pulse energy  $E(\nu)$  to account for variation of the laser power and to approximate the infrared absorption cross section

$$\sigma(\nu) = D(\nu)/E(\nu) \quad (3)$$

The FEL laser pulse energy is reconstructed by measuring the pulse energy of a fraction of the pulse that is outcoupled of the FELICE cavity.<sup>23</sup> Typical pulse energies range from 1000 mJ at 400 cm<sup>-1</sup> to 200 mJ at 1600 cm<sup>-1</sup>.

**Theoretical.** Five structures of C<sub>60</sub>V<sup>+</sup>, i.e.,  $\eta^5$ ,  $\eta^6$ ,  $\eta^{2(6-6)}$ ,  $\eta^{2(5-6)}$ , and  $\eta^1$  have been fully optimized to obtain the most probable binding site of the vanadium ion on the C<sub>60</sub> surface. Endohedral structures are not considered as the experiments start with preformed C<sub>60</sub>, while it is known that the activation energy for a metal atom entering into the C<sub>60</sub> cage is significant.<sup>36</sup> Six functionals, i.e., BPW91, PBE, PBE0, B3LYP, M06-2X, and  $\omega$ B97XD, have been employed to justify the reliability of density functional theory (DFT) calculations. All of these functionals calculate the structure in the  $S = 2$  spin state to be most stable (Table S1). From the comparison in Figure S10, it can be seen that BPW91 gives the highest cosine similarity score in comparison with the experiment without applying any scaling factors, consistent with our previous findings on the good performance of BPW91 in simulating the infrared spectra of C<sub>60</sub>V<sup>+</sup>(H<sub>2</sub>O)<sub>1,2</sub> complexes.<sup>20,21</sup> Due

to the large size of the studied complex, double- $\zeta$  quality basis sets (6-31G(d) and/or def2-SVP, see details in the text) were used for all calculations. Triple- $\zeta$  quality basis sets (6-311G(d), def2-TZVP, and LanL2TZ) were also checked, showing consistent results with the double- $\zeta$  basis sets (Figure S11). The harmonic approximation was employed to perform vibrational analysis of the calculated structures. The vibrational analysis is used on the one hand to confirm that the calculated structures are real minima for ground states or have only one imaginary frequency for transition states and on the other hand to simulate theoretical IR spectra to compare with the measured IR(M)PD spectra. All of the calculations were conducted with the Gaussian09 program package.<sup>37</sup> Energy decomposition analysis (EDA),<sup>38</sup> performed with the ADF 2020 software package,<sup>39</sup> was carried out at the BP86+D3(BJ)/TZ2P level to partition the bonding interaction energy  $\Delta E_{\text{int}}$  between V<sup>+</sup> and C<sub>60</sub> into orbital ( $\Delta E_{\text{orb}}$ ) and electrostatic ( $\Delta E_{\text{elstat}}$ ) interactions, Pauli repulsion ( $\Delta E_{\text{Pauli}}$ ), and dispersion ( $\Delta E_{\text{disp}}$ ). The natural orbitals for chemical valence (NOCV) can decompose the orbital interaction term  $\Delta E_{\text{orb}}$  into pairwise contributions, and plots of deformation densities were used to visualize the electron transfer caused by orbital interaction.<sup>40,41</sup>

Born–Oppenheimer molecular dynamics (BOMD) simulations were carried out under canonical ensemble (NVT) using the PBE functional with the D3 dispersion correction<sup>42</sup> as implemented in the CP2K code.<sup>43</sup> The DZVP-MOLOPT-SR-GTH basis set was used in conjunction with Geodecker, Teter, and Hutter (GTH) pseudopotentials<sup>44</sup> with a plane-wave cutoff energy of 300 Ry and a REL\_CUTOFF of 40 Ry. The three orthorhombic lattice constants were set as 25 Å to avoid lateral interactions between the periodic images. The total simulation time was 5 ps with 1 fs per step.

**Cosine Similarity Score.** To quantitatively assess the agreement between the calculated and experimental infrared spectra, we employed the recently proposed cosine similarity score.<sup>26–28</sup> In this method, the similarity is quantified as the cosine of the angle  $\theta$  between two  $n$ -dimensional vectors, calculated using their normalized Euclidean dot product

$$\cos(\theta) = \frac{\mathbf{A} \cdot \mathbf{B}}{\|\mathbf{A}\| \|\mathbf{B}\|} = \frac{\sum_{i=1}^n A_i B_i}{\sqrt{\sum_{i=1}^n A_i^2} \cdot \sqrt{\sum_{i=1}^n B_i^2}}$$

where  $\mathbf{A}$  and  $\mathbf{B}$  are two  $n$ -dimensional vectors with elements  $A_i$  and  $B_i$ . This method assesses the degree to which the two vectors representing the experimental and theoretical spectra in this case are parallel. The outcomes range from 0 to 1, where a cosine value closer to 1 indicates a higher similarity. The intensity values in the computed spectrum are evaluated at the exact wavenumbers of the experimental spectrum so that the two spectra have a common  $x$ -axis. To take into account possible anharmonic corrections for the calculated harmonic frequencies, the calculated spectra can be scaled before calculating the cosine similarity scores.

Kempkes et al.<sup>27</sup> proposed a slightly modified version of the above formula to make the cosine similarity scores more sensitive to the frequency overlap between bands in  $\mathbf{A}$  and  $\mathbf{B}$ , and less to the deviations in their peak intensities. That may partially eliminate the potential effects of tagging and/or multiple photon absorption on the measured intensities. Both the experimental and calculated spectra are scaled to a maximum intensity of 1 and then the logarithm of these scaled values is taken as

$$A_i^{\text{rev}} = \log\left(\frac{A_i}{A_{\max}} + c\right)$$

where  $c$  is a constant that is identical for vectors  $\mathbf{A}$  and  $\mathbf{B}$ . The value of  $c$  is a compromise between being sensitive to low-intensity bands in the spectrum, on the one hand, and avoiding experimental noise affecting the similarity, on the other hand. We followed this approach in the current work and used a  $c$  value of 0.71 by testing a small set of experimental and computational spectra to give the best results.

## ASSOCIATED CONTENT

### SI Supporting Information

The Supporting Information is available free of charge at <https://pubs.acs.org/doi/10.1021/jacs.3c08451>.

Simulated infrared spectra of  $C_{60}V^+$  with and without Ar tag; comparison of the experimental spectrum with simulated ones; snapshots showing the location changes of V during BOMD simulations; relative stabilities and averaged V–C distances of the four isomers of  $C_{60}V^+$ ; Cartesian coordinates of the four isomers of  $C_{60}V^+$  at the BPW91/6-31G(d) level; and additional theoretical results ([PDF](#))

Trajectories of the BOMD simulations ([ZIP](#))

## AUTHOR INFORMATION

### Corresponding Authors

Ewald Janssens — *Quantum Solid-State Physics, KU Leuven, 3001 Leuven, Belgium;* [ORCID iD](https://orcid.org/0000-0002-5945-1194); Email: [ewald.janssens@kuleuven.be](mailto:ewald.janssens@kuleuven.be)

Gao-Lei Hou — *MOE Key Laboratory for Non-Equilibrium Synthesis and Modulation of Condensed Matter, School of Physics, Xi'an Jiaotong University, Xi'an 710049 Shaanxi, China;* [ORCID iD](https://orcid.org/0000-0003-1196-2777); Email: [gaolei.hou@xjtu.edu.cn](mailto:gaolei.hou@xjtu.edu.cn)

### Authors

Jianzhi Xu — *MOE Key Laboratory for Non-Equilibrium Synthesis and Modulation of Condensed Matter, School of Physics, Xi'an Jiaotong University, Xi'an 710049 Shaanxi, China*

Joost M. Bakker — *Radboud University, Institute for Molecules and Materials, FELIX Laboratory, 6525 ED Nijmegen, The Netherlands;* [ORCID iD](https://orcid.org/0000-0002-1394-7661)

Olga V. Lushchikova — *Radboud University, Institute for Molecules and Materials, FELIX Laboratory, 6525 ED Nijmegen, The Netherlands;* [ORCID iD](https://orcid.org/0000-0002-5699-6818)

Peter Lievens — *Quantum Solid-State Physics, KU Leuven, 3001 Leuven, Belgium*

Complete contact information is available at: <https://pubs.acs.org/10.1021/jacs.3c08451>

### Author Contributions

The original data that support the findings of this study are available from the corresponding author upon reasonable request.

### Notes

The authors declare no competing financial interest.

## ACKNOWLEDGMENTS

This work was supported by National Natural Science Foundation of China (92261101), the Innovation Capability Support Program of Shaanxi Province (2023-CX-TD-49), and the KU Leuven Research Council (project C14/22/103 and KA/20/045). G.-L.H. acknowledges the support from the “Young Talent Support Plan” of Xi'an Jiaotong University, the “Selective Funding Project for Overseas Student Scientific and Technological Activities” of Shaanxi province, as well as the Fundamental Research Funds for Central Universities, China. Part of the computational resources and services used in this work were provided by the VSC (Flemish Supercomputer Center), funded by the Research Foundation—Flanders

(FWO) and the Flemish Government—department EWI. The authors gratefully acknowledge the Nederlandse Organisatie voor Wetenschappelijk Onderzoek (NWO) for the support of the FELIX Laboratory and thank the FELIX staff. G.-L.H. gratefully acknowledges Prof. Su-Yuan Xie from Xiamen University for inspiring and encouraging discussions during the preparation of this manuscript.

## REFERENCES

- (1) Kroto, H. W.; Heath, J. R.; O'Brien, S. C.; Curl, R. F.; Smalley, R. E.  $C_{60}$ : Buckminsterfullerene. *Nature* **1985**, *318*, 162–163.
- (2) Kroto, H. W.; Allaf, A. W.; Balm, S. P.  $C_{60}$ : Buckminsterfullerene. *Chem. Rev.* **1991**, *91*, 1213–1235.
- (3) Acquah, S. F. A.; Penkova, A. V.; Markelov, D. A.; Semisalova, A. S.; Leonhardt, B. E.; Magi, J. M. Review-The Beautiful Molecule: 30 Years of  $C_{60}$  and Its Derivatives. *ECS J. Solid State Sci. Technol.* **2017**, *6*, M3155–M3162.
- (4) Hebard, A. F.; Rosseinsky, M. J.; Haddon, R. C.; Murphy, D. W.; Glarum, S. H.; Palstra, T. T. M.; Ramirez, A. P.; Kortan, A. R. Superconductivity at 18 K in potassium-doped  $C_{60}$ . *Nature* **1991**, *350*, 600–601.
- (5) Chandrasekhar, K. R. S.; Ghosh, S. K. Alkali-Metal-Induced Enhancement of Hydrogen Adsorption in  $C_{60}$  Fullerene: An ab Initio Study. *Nano Lett.* **2008**, *8*, 13–19.
- (6) Yoon, M.; Yang, S.; Hicke, C.; Wang, E.; Geohegan, D.; Zhang, Z. Calcium as the Superior Coating Metal in Functionalization of Carbon Fullerenes for High-Capacity Hydrogen Storage. *Phys. Rev. Lett.* **2008**, *100*, 206806.
- (7) Lebedeva, M. A.; Chamberlain, T. W.; Khlobystov, A. N. Harnessing the Synergistic and Complementary Properties of Fullerene and Transition-Metal Compounds for Nanomaterial Applications. *Chem. Rev.* **2015**, *115*, 11301–11351.
- (8) Chen, Y.-C.; Hsu, C.-Y.; Lin, R. Y.-Y.; Ho, K.-C.; Lin, J. T. Materials for the Active Layer of Organic Photovoltaics: Ternary Solar Cell Approach. *ChemSusChem* **2013**, *6*, 20–35.
- (9) Park, H.; Park, J.; Lim, A. K. L.; Anderson, E. H.; Alivisatos, A. P.; McEuen, P. L. Nanomechanical oscillations in a single- $C_{60}$  transistor. *Nature* **2000**, *407*, 57–60.
- (10) Yee, S. K.; Malen, J. A.; Majumdar, A.; Segalman, R. A. Thermoelectricity in Fullerene-Metal Heterojunctions. *Nano Lett.* **2011**, *11*, 4089–4094.
- (11) Shukla, M. K.; Dubey, M.; Leszczynski, J. Theoretical Investigation of Electronic Structures and Properties of  $C_{60}$ -Gold Nanocontacts. *ACS Nano* **2008**, *2*, 227–234.
- (12) Goulart, M.; Kuhn, M.; Martini, P.; Chen, L.; Hagelberg, F.; Kaiser, A.; Scheier, P.; Ellis, A. M. Highly Stable  $[C_{60}AuC_{60}]^\pm$  Dumbbells. *J. Phys. Chem. Lett.* **2018**, *9*, 2703–2706.
- (13) Sankar De, D.; Flores-Livas, J. A.; Saha, S.; Genovese, L.; Goedecker, S. Stable structures of exohedrally decorated  $C_{60}$ -fullerenes. *Carbon* **2018**, *129*, 847–853.
- (14) Kröger, H.; Reinke, P.; Büttner, M.; Oelhafen, P. Gold cluster formation on a fullerene surface. *J. Chem. Phys.* **2005**, *123*, 114706.
- (15) Lyon, J. T.; Andrews, L. Infrared Spectrum of the Au- $C_{60}$  Complex. *ChemPhysChem* **2005**, *6*, 229–232.
- (16) Zeng, Q.; Chu, X.; Yang, M.; Wu, D.-Y. Spin-orbit coupling effect on Au- $C_{60}$  interaction: A density functional theory study. *Chem. Phys.* **2012**, *395*, 82–86.
- (17) Basiuk, V. A.; Borys-Sosa, P. A. Interaction of Au Atom with Fullerene  $C_{60}$ : Performance of DFT Functionals Incorporated into the DMol3Module. *J. Comput. Theor. Nanosci.* **2013**, *20*, 328–333.
- (18) Nagao, S.; Kurikawa, T.; Miyajima, K.; Nakajima, A.; Kaya, K. Formation and Structures of Transition Metal- $C_{60}$  Clusters. *J. Phys. Chem. A* **1998**, *102*, 4495–4500.
- (19) Robledo, M.; Aguirre, N. F.; Díaz-Tendero, S.; Martín, F.; Alcamí, M. Bonding in exohedral metal-fullerene cationic complexes. *RSC Adv.* **2014**, *4*, 53010–53020.
- (20) Hou, G. L.; Yang, T.; Li, M.; Vanbuel, J.; Lushchikova, O. V.; Ferrari, P.; Bakker, J. M.; Janssens, E. Water Splitting by  $C_{60}$ -

- Supported Vanadium Single Atoms. *Angew. Chem., Int. Ed.* **2021**, *60*, 27095–27101.
- (21) Li, M.; Yang, T.; Bakker, J. M.; Janssens, E.; Hou, G.-L. Unveiling the role of  $C_{60}$ -supported vanadium single atoms for catalytic overall water splitting. *Cell Rep. Phys. Sci.* **2022**, *3*, 100910.
- (22) German, E.; Hou, G.-L.; Vanbuel, J.; Bakker, J. M.; Alonso, J. A.; Janssens, E.; López, M. J. Infrared spectra and structures of  $C_{60}Rh_n^+$  complexes. *Carbon* **2022**, *197*, 535–543.
- (23) Hou, G.-L.; Lushchikova, O. V.; Bakker, J. M.; Lievens, P.; Decin, L.; Janssens, E. Buckyball-metal complexes as potential carriers of astronomical unidentified infrared emission bands. *Astrophys. J.* **2023**, *952*, 13.
- (24) Bakker, J. M.; Lapoutre, V. J. F.; Redlich, B.; Oomens, J.; Sartakov, B. G.; Fielicke, A.; von Helden, G.; Meijer, G.; van der Meer, A. F. G. Intensity-resolved IR multiple photon ionization and fragmentation of  $C_{60}$ . *J. Chem. Phys.* **2010**, *132*, 074305.
- (25) Gerlich, D. Infrared spectroscopy of cold trapped molecular ions using He-tagging. *J. Chin. Chem. Soc.* **2018**, *65*, 637–653.
- (26) Fu, W.; Hopkins, W. S. Applying Machine Learning to Vibrational Spectroscopy. *J. Phys. Chem. A* **2018**, *122*, 167–171.
- (27) Kempkes, L. J. M.; Martens, J.; Berden, G.; Houthuijs, K. J.; Oomens, J. Investigation of the position of the radical in z3-ions resulting from electron transfer dissociation using infrared ion spectroscopy. *Faraday Discuss.* **2019**, *217*, 434–452.
- (28) Müller, F.; Stuckrath, J. B.; Bischoff, F. A.; Gagliardi, L.; Sauer, J.; Debnath, S.; Jorewitz, M.; Asmis, K. R. Valence and Structure Isomerism of  $Al_2FeO_4^+$ : Synergy of Spectroscopy and Quantum Chemistry. *J. Am. Chem. Soc.* **2020**, *142*, 18050–18059.
- (29) Jerabek, P.; Schwerdtfeger, P.; Frenking, G. Dative and electron-sharing bonding in transition metal compounds. *J. Comput. Chem.* **2019**, *40*, 247–264.
- (30) Campbell, E. K.; Holz, M.; Gerlich, D.; Maier, J. P. Laboratory confirmation of  $C_{60}^+$  as the carrier of two diffuse interstellar bands. *Nature* **2015**, *523*, 322–323.
- (31) Krełowski, J. Diffuse Interstellar Bands. A Survey of Observational Facts. *Publ. Astron. Soc. Pac.* **2018**, *130*, 071001.
- (32) Ferrari, P.; Vanbuel, J.; Liao, T.-W.; Li, Y.; Janssens, E.; Lievens, P., The Double Laser Ablation Source Approach. In *Gas Aggregation Synthesis of Nanoparticles*. In *Modifications of Gas Aggregation Sources*, Huttel, Y., Ed. Wiley-VCH, Weinheim: 2017; pp 59–78.
- (33) Vanbuel, J.; German, E.; Libeert, G.; Veys, K.; Moens, J.; Alonso, J. A.; Lopez, M. J.; Janssens, E. Reactivity of Cobalt-Fullerene Complexes towards Deuterium. *ChemPhysChem* **2020**, *21*, 1012–1018.
- (34) Roithová, J.; Gray, A.; Andris, E.; Jašík, J.; Gerlich, D. Helium Tagging Infrared Photodissociation Spectroscopy of Reactive Ions. *Acc. Chem. Res.* **2016**, *49*, 223–230.
- (35) Yang, N.; Duong, C. H.; Kelleher, P. J.; McCoy, A. B.; Johnson, M. A. Deconstructing water's diffuse OH stretching vibrational spectrum with cold clusters. *Science* **2019**, *364*, 275–278.
- (36) Fye, J. L.; Jarrold, M. F. Ion mobility studies of metal-coated fullerenes. *Int. J. Mass Spectrom.* **1999**, *185–187*, 507–515.
- (37) Frisch, M. J.; Trucks, G. W.; Schlegel, H. B.; Scuseria, G. E.; Robb, M. A.; Cheeseman, J. R.; Scalmani, G.; Barone, V.; Petersson, G. A.; Nakatsuji, H.; Li, X.; Caricato, M.; Marenich, A. V.; Bloino, J.; Janesko, B. G.; Gomperts, R.; Mennucci, B.; Hratchian, H. P.; Ortiz, J. V.; Izmaylov, A. F.; Sonnenberg, J. L.; Williams-Young, D.; Ding, F.; Lipparini, F.; Egidi, F.; Goings, J.; Peng, B.; Petrone, A.; Henderson, T.; Ranasinghe, D.; Zakrzewski, V. G.; Gao, J.; Rega, N.; Zheng, G.; Liang, W.; Hada, M.; Ehara, M.; Toyota, K.; Fukuda, R.; Hasegawa, J.; Ishida, M.; Nakajima, T.; Honda, Y.; Kitao, O.; Nakai, H.; Vreven, T.; Throssell, K.; J A Montgomery, J.; Peralta, J. E.; Ogliaro, F.; Bearpark, M. J.; Heyd, J. J.; Brothers, E. N.; Kudin, K. N.; Staroverov, V. N.; Keith, T. A.; Kobayashi, R.; Normand, J.; Raghavachari, K.; Rendell, A. P.; Burant, J. C.; Iyengar, S. S.; Tomasi, J.; Cossi, M.; Millam, J. M.; Klene, M.; Adamo, C.; Cammi, R.; Ochterski, J. W.; Martin, R. L.; Morokuma, K.; Farkas, O.; Foresman, J. B.; Fox, D. J. *Gaussian 09*, revision E.01; Gaussian, Inc: Wallingford CT, 2013.
- (38) Ziegler, T.; Rauk, A. CO, CS,  $N_2$ ,  $PF_3$ , and  $CNCH_3$  as Donors and  $\pi$  Acceptors. A Theoretical Study by the Hartree-Fock-Slater Transition-State Method. *Inorg. Chem.* **1979**, *18*, 1755–1759.
- (39) Baerends, E. J.; Ziegler, T.; Autschbach, J.; Bashford, D.; Béres, A.; Bickelhaupt, F.; Bo, C.; Boerrigter, P.; Cavallo, L.; Chong, D. *ADF2020 SCM, Theoretical Chemistry*; Vrije Universiteit: Amsterdam, the Netherlands,: 2020.
- (40) Michalak, A.; Mitoraj, M.; Ziegler, T. Bond orbitals from chemical valence theory. *J. Phys. Chem. A* **2008**, *112*, 1933–1939.
- (41) Mitoraj, M. P.; Michalak, A.; Ziegler, T. A combined charge and energy decomposition scheme for bond analysis. *J. Chem. Theory Comput.* **2009**, *5*, 962–975.
- (42) Grimme, S.; Antony, J.; Ehrlich, S.; Krieg, H. A consistent and accurate ab initio parametrization of density functional dispersion correction (DFT-D) for the 94 elements H-Pu. *J. Chem. Phys.* **2010**, *132*, 154104.
- (43) Kühne, T. D.; Iannuzzi, M.; Del Ben, M.; Rybkin, V. V.; Seewald, P.; Stein, F.; Laino, T.; Khalil, R. Z.; Schutt, O.; Schiffmann, F.; Golze, D.; Wilhelm, J.; Chulkov, S.; Bani-Hashemian, M. H.; Weber, V.; Borstnik, U.; Taillefumier, M.; Jakobovits, A. S.; Lazzaro, A.; Pabst, H.; Muller, T.; Schade, R.; Guidon, M.; Andermatt, S.; Holmberg, N.; Schenter, G. K.; Hehn, A.; Bussy, A.; Belleflamme, F.; Tabacchi, G.; Gloss, A.; Lass, M.; Bethune, I.; Mundy, C. J.; Plessl, C.; Watkins, M.; VandeVondele, J.; Krack, M.; Hutter, J. CP2K: An electronic structure and molecular dynamics software package - Quickstep: Efficient and accurate electronic structure calculations. *J. Chem. Phys.* **2020**, *152*, 194103.
- (44) Goedecker, S.; Teter, M.; J. H. Separable dual-space Gaussian pseudopotentials. *Phys. Rev. B* **1996**, *54*, 1703–1710.